

---

# Determining Geometric Grain Structure from X-Ray Micro-Tomograms of Gradated Soil

Ulrike Homberg<sup>1</sup>, Richard Binner<sup>2</sup>, Steffen Prohaska<sup>1</sup>, Vincent J. Dercksen<sup>1</sup>, Anja Kuß<sup>1</sup> and Ute Kalbe<sup>2</sup>

<sup>1</sup> Zuse Institute Berlin (ZIB) [homberg|prohaska|dercksen|kuss@zib.de](mailto:homberg|prohaska|dercksen|kuss@zib.de)

<sup>2</sup> Federal Institute for Materials Research and Testing (BAM) [richard.binner|ute.kalbe@bam.de](mailto:richard.binner|ute.kalbe@bam.de)

**Summary.** We present a method to determine the geometric grain structure of gradated soil by means of X-ray micro-computed tomography and image processing. High-resolution tomographic images are acquired of sample material that is embedded in epoxy resin. Position and shape of coarse- and medium-sized grains are computed by applying morphologic image operators. We compare the results of image processing with the grain size distribution measured by sieving. First results indicate that our method has the potential of analysing the structure formed by grains of size 1 *mm* to 20 *mm*, although more data are needed to confirm this statistically. Our findings suggest that computed tomography in combination with automatic image processing methods can deliver geometric parameters of real grain and pore structure suitable for analysing suffosive erosion phenomena.

**Key words:** gradated soil, suffosive erosion phenomena, pore and grain structure, micro computed tomography, morphologic image processing

## 1 Introduction

Gradated soils are defined as coarse grained soils that exhibit an asymmetric grain size distribution. They are frequently at risk to be suffosive, especially if they feature a gap grading. Figure 1 illustrates a typical grain size distribution of a suffosive non-cohesive soil with a gap grading between 0.63 and 2.8 *mm*. Suffosion characterises the relocation and discharge of fine particles by pore water flow. Suffosion does not change the supporting granular structure, but increases the porosity and therefore the permeability of the soil. However a proceeding suffosion and additional external mechanical influences might cause instability of the supporting granular structure and finally soil erosion [2, 6, 25, 39]. These processes are important in the field of soil and water engineering, e.g. for road and dyke construction or mining activities [4, 5, 24, 26, 36].

The hitherto existing suffosion criteria are based on surveys that have been developed for the dimensioning of natural filters (soil filters) to be used in dam construction. Fundamental geometrical suffosion criteria using the grain size distributions of soils as input parameters were developed amongst others by [2, 14, 18]. The relationship between suffosion susceptibility and the permeability or grain size distribution was investigated by [32] and [17]. Most of

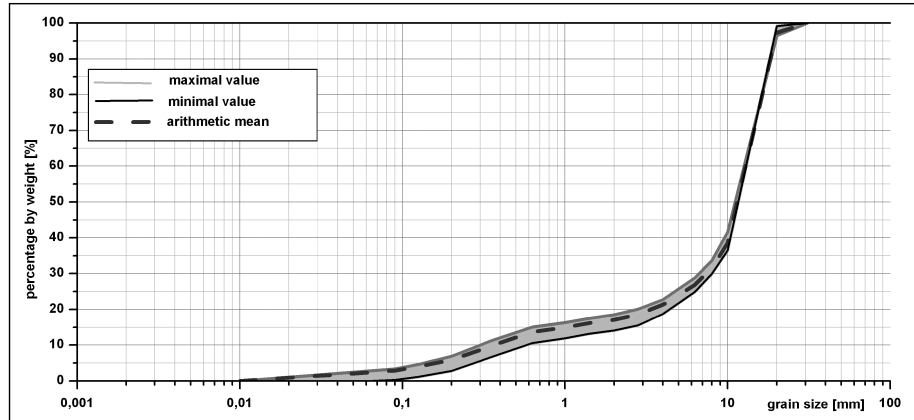


Fig. 1. Grain size distribution of the investigated soil including standard deviation ( $n=8$ ).

the outcomes regarding understanding of suffosion mechanisms have been derived from experimental work. A simplified mathematical relationship to describe the whole pore structure was developed, e.g. by [40].

Considering 3D geometry of pore structure, although not easy for real soils, would support our understanding of suffosion. Today, there are only a few studies that regard the 3D pore geometry (e.g. [19, 37]). A more realistic approach taking into account the spatial pore structure generated by grains of irregular shape and the specific grain size distribution of suffusive soils based on the investigation of undisturbed samples is needed. The determined parameters of the grain structure will be used to calibrate the simulations of transport and clogging processes with pore networks and correlated percolation models.

This work presents a method that uses X-ray micro-computed tomography followed by automatic image processing to reconstruct the geometric grain structure of soil. Our sample preparation captures the situation in real gradated soil as good as possible, although the soil specimens are not taken from a real site. We are able to reconstruct position, shape and volume of grains larger than 1 mm with promising quality. The processing is validated by comparison with the grain size distribution known from sieving. In the following we discuss related work, present our sample preparation and data acquisition technique, give details on the image analysis, present results and discuss them, before we conclude that our method is a promising approach for determining the geometric parameters of real soil, suitable for analysing suffosion processes.

## 2 Related Work

X-ray computerised tomography (CT) has become a common technique to study the structure of materials. A great advantage of this technique is that it provides insight in the 3D structure in a non-destructive manner. In recent years, CT has for example been used to study the micro-structure of asphalt concrete (see e.g. [23]), cement concrete [16], rock [33] and soil [22] and of soil colloids [31].

Analysing the grain structure in micro-CT scans of soil samples of a specific grain size distribution requires the processing of large data containing a large number of touching grains. Additionally, the grains may be of different size and different shape. A frequently used pipeline for segmenting multiple, possibly touching, granular objects from image data, in particular CT images, consists of the following steps. In an initial thresholding step, the foreground is separated from the background. In the second step, the grains are labeled individually. This is achieved using watershed segmentation for defining the grain regions.

These image processing steps are used with modifications by different authors to achieve different research goals. For example, Ghalib et al. [10] present an approach based on thresholding and watershedding onto the distance field of the objects in order to find the individual particles within 2D mosaic images. Kim et al. [15] extract number, shape and size of particles, such as stone aggregates, from Laser Profiling images. For extracting individual particles they use watershed segmentation based on edges in the image, identified by the Canny edge detector. The particles had to be separated before scanning. Kaestner [13] identifies interfaces between two homogeneous sand materials in 3D images from CT using a similar segmentation technique to segment the sand materials. A subsequent classification algorithm then finds the interface between different types of material. Al-Raousha [1] extracts structures of equally sized glass beads in CT images in order to compute the local void ratio (porosity). Razavi [22] extracts spherical and elongated beads and grains from CT images in order to estimate the representative elementary volume (REV) of granular materials based on marker-based watershed segmentation using regional maxima of the distance field as markers.

There are, of course, also other approaches to the segmentation problem, e.g. wavelet- [28] or classifier-based [38] approaches.

To our knowledge, no papers are published that deal with the automatic segmentation and identification of a massive amount of grains of different shapes and different sizes in large high-resolution 3D CT images in order to describe the grain structure geometrically.

### 3 Sample Preparing and Data Acquisition

In order to record adequate CT datasets of specimens of suffosive soil material some prerequisites need to be fulfilled. First, the specimens should represent the natural bedding and compactness of the suffosive material as realistic as possible. Second, the specimen volume should be appropriate and stable. Different procedures (e.g. resin embedding, compacting) were tested in order to assemble suitable specimens. In the chosen preparing procedure the sample material will be divided, compacted and embedded in epoxy resin. The individual steps are: 1) Dividing the material into aliquots of approximately 50g portions using a sample splitter according to [7] and [8]. 2) Filling the sub-samples into a column in layers. 3) Compacting using the vibration of a sieving machine and plunger, in the meantime rotating the column in defined time intervals. 4) Embedding the specimen in epoxy resin. 5) Cutting the hardened cylindrical specimen to the optimal size of diameter 60 mm and height 60 mm (the larger the sample the lower the CT resolution).

The grain size distribution of the investigated soil is determined by means of dry sieving. The standard deviation of sieving is calculated from eight replicates in order to estimate the sieving error (Figure 1).

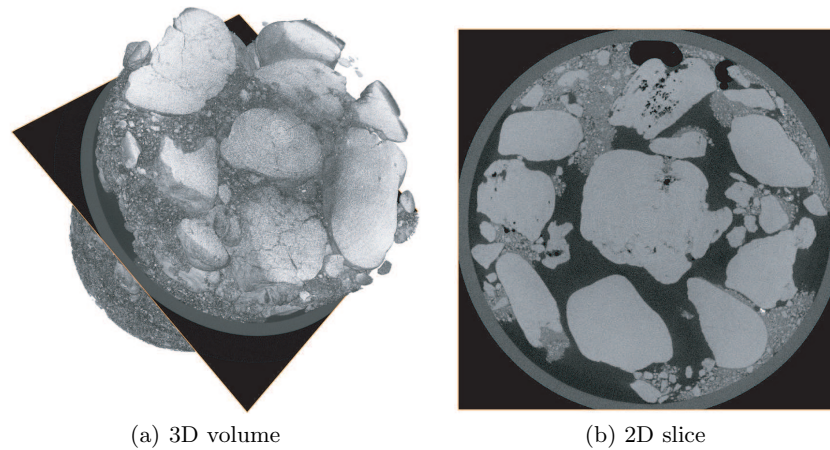


**Fig. 2.** Original data from a CT scan of a sample of size  $60 \times 60 \text{ mm}$ .

Morphological features are visualised using 3D Cone Beam Tomography based on undisturbed core samples. The used tomography device was developed at the Federal Institute for Materials Research and Testing (BAM) and uses an X-ray tube (tungsten anode) with a microfocal spot (about  $10 \text{ \AA}$ ), together with a combination of an image intensifier and a CCD camera as detection system. The measurement of the samples is performed at  $205 \text{ kV}$  and  $80 \text{ \mu A}$  using a  $1.0 \text{ mm Cu}$  and  $0.25 \text{ mm Ag}$  pre-filter to reduce the effect of beam hardening. The voltage in relation to the X-ray current intensity determines the resolution. The resolution of the used CT system is  $20\text{--}50 \text{ \mu m}$  depending on the size of the investigated sample. If the size of a sample (e.g. length) exceeds its diameter, several measurements at different heights will be performed and the resulting images will be combined. Figure 2 depicts an example result. On the left, the complete 3D dataset is visualised, whereas on the right only one slice of the dataset is presented.

## 4 Image Analysis

The goal of our approach is to obtain geometric information about the grain structure from the three-dimensional micro-CT data of the prepared soil samples. Therefore, it is necessary to detect the grains and determine their volume and number. A complicating factor is that clusters of touching objects appear in the data, which have to be separated in order to obtain reliable results.

The specimens contains grains of size  $10 \text{ \mu m}$  to  $20 \text{ mm}$ . At a resolution of  $35 \text{ \mu m}$  per voxel, this leads to a grain extent of less than one voxel up to circa 570 voxels per grain. We use a size-dependent partitioning of the grains in our analysis method, as the individual grains can be better detected by using the specific morphological properties of the fraction they belong to. Therefore, we define three groups of structures:

- **Fine structures.** Grains with a diameter smaller than 4 voxels ( $150 \text{ \mu m}$ ) are extremely difficult to distinguish. Such grains appear as blurry regions, due to the resolution limit

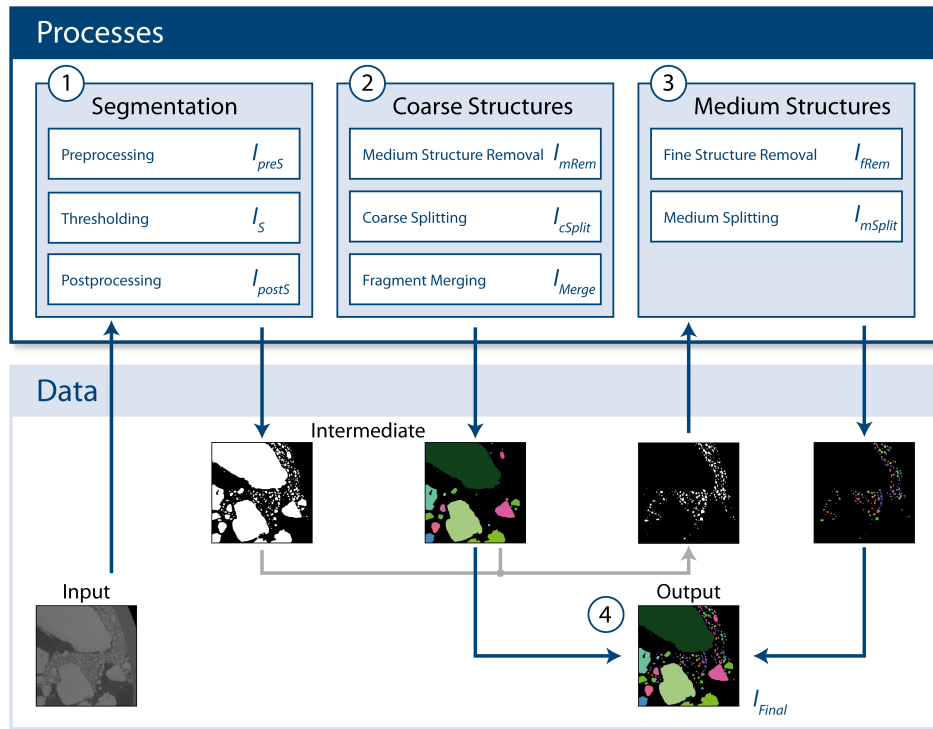


**Fig. 3.** Pipeline of processing steps. In four steps the structures are segmented, extracted depending on their size and combined to a final result.

and the partial volume effect. As such grains cannot be reliably extracted, we exclude them from our analysis.

- **Medium structures.** We define medium-sized grains as grains with a diameter of  $150 - 500 \mu m$ . They are large enough to be detected and are generally of roundish shape.
- **Coarse structures.** Large grains have a wide variety of potentially complex shapes, and often exhibit intragranular pores and cracks. The lower bound of  $500 \mu m$  for the diameter of grains belonging to this fraction has been determined experimentally.

Based on the partitioning, we present an analysis pipeline consisting of four steps (Fig. 3):

1. Segmentation of the grain structure
2. Extraction of coarse structures
3. Extraction of medium structures
4. Merging extraction results

## 4.1 Segmentation

The aim of the first step in the pipeline, the segmentation step, is to create a binary image separating foreground objects from the background. The soil and the epoxy resin appear as distinct gray-value intervals in the CT images. Therefore, a simple thresholding with pre- and post-processing can be used for segmentation.

The pre-processing step consists of two filter operations. First, we apply a sigmoid filter [11] in order to enhance the contrast at the boundary between the soil and the epoxy resin. The sigmoid filter is defined as:

$$S(I) = (Max - Min) \frac{1}{(1 + e^{-\frac{I-\beta}{\alpha}})} + Min \quad (1)$$

where  $I$  is the input image and  $S(I)$  is the output image. The sigmoid filter enhances the contrast in a range of interest, centered around  $\beta$  and with a width controlled by  $\alpha$ . This enhancement occurs at the cost of the contrast outside this range.  $Min$  and  $Max$  are the minimum and maximum of the output range (normally [0,255]). Our range of interest is the boundary between soil and epoxy resin, so we set  $\beta$  to the value of the valley between the histogram peaks corresponding to these materials. The value for  $\alpha$  is set according to the width of this valley.

Second, we use a median filter [3] of size  $3 \times 3 \times 3$  in order to reduce noise. This combination of filters allows for a global threshold to be used for segmentation.

The global threshold segmentation classifies each voxel as belonging to the foreground (value 1), representing the grain structure, or as belonging to the background (value 0). The threshold value  $T$  is set at the onset of the slope of the histogram peak corresponding to the soil, the precise location is determined by systematic testing.

In a post-processing step, intragranular pores are removed to avoid errors in the following algorithms. The pores to be removed are sets of connected background voxels, entirely surrounded by foreground voxels. They are found by floodfilling all background regions which touch the image border. All voxels which have not been flooded and which are not part of the foreground are classified as holes and removed, i.e. they are added to the foreground.

The binary image  $I_{postS}$ , resulting from this segmentation, now forms the basis for the following steps of our pipeline.

## 4.2 Extraction of coarse structures

To analyse the grain structure, it is necessary to extract all grains from the segmentation result  $I_{postS}$ , thereby splitting touching objects and assigning each grain a distinct label. In the second part of the pipeline, the *coarse* structures are identified. In order to do this, the medium and fine structures are to be discarded.

### *Removal of fine and medium structures*

For analysing the coarse structure we remove medium and fine objects. Objects are defined as regions of 6-connected foreground voxels. We use the volume of objects, i.e. the number

of voxels in the region, as a criterion for removal. To obtain the coarse structures, we remove all objects with a volume of less than  $V_{coarse}^{min} = 1500$  voxels. For data with a resolution of  $35 \mu m$  and assuming spherical object shape, this value corresponds to grains with a radius of approximately  $500 \mu m$ . However, there exist clusters comprised of small, touching objects. Their volumes may each exceed  $V_{coarse}^{min}$ , which would classify an entire cluster as a single coarse object. We first split such clusters by a slightly modified morphological opening by reconstruction operation [29]. The first step of this operation is an erosion [29] of sufficient size (4 steps), such that clusters of medium and small objects are splitted. The second step is a geodesic dilation [29] of such a size (5 steps) that the original volume of the eroded objects is restored, without restoring the links between the formerly touching objects. After this operation, the objects with volume smaller than  $V_{coarse}^{min}$  are discarded. This results in a binary image  $I_{mRemove}$  containing the coarse structures.

### *Coarse Splitting*

In this step, all individual coarse objects in the image  $I_{mRemove}$  are identified and labeled. Therefore, touching objects first have to be separated. The area of contact between touching coarse grains is larger than for smaller grains. This property is used in the following approach to separate such objects.

1. The clusters are split by an erosion of sufficient size. This size must be large enough to remove areas of contact between touching objects, but must not be of such size that individual grains are completely removed. We used an erosion of size 7, i.e. 7 subsequent erosions with a 6-connected structuring element. The objects have now been split, but are also significantly reduced in volume, which would cause errors in the computation of the grain's geometric information.
2. The separated regions are identified by assigning all voxels of a region the same label.
3. In order to restore the volume, we perform a modified morphological reconstruction [29]. Repeated geodesic dilation steps are performed on all objects in the labeled image simultaneously, using  $I_{mRemove}$  as mask. The labeled regions thus increasingly recover their original volume, but remain within the foreground  $I_{mRemove}$ . Whenever differently labeled regions are about to touch, a single voxel wide boundary is retained, and marked as such. These boundary voxels are used in the next step.

The *coarseSplitting* method thus results in a labeled image  $I_{cSplit}$ , identifying voxels of each coarse object and voxels of common object boundaries.

### *Merging fragments*

The splitting result contains several fragmented objects. These are mainly caused by micro-cracks in these objects. In this step, such fragmented regions are to be merged, while keeping the separation between completed objects.

Whereas the boundary area of two correctly separated grains is usually small, grains which have been incorrectly split (fragments) have a large boundary area in comparison to the fragment volume. In order to merge fragmented objects, we consider all pairs of objects

sharing a common boundary and define an algorithm based on the ratio between the shared boundary area and the object volumes to decide whether to merge each pair:

1. For two objects,  $A$  and  $B$ , with a common boundary  $A_{AB}$ , the size (in voxels) of  $A_{AB}$  is computed.
2. The distance transform inside both object regions is computed. The distance maximum inside each object represents the maximal radius,  $r_A$  and  $r_B$  resp., of the objects. If the objects were spheres, the objects would be considered separate if the contact area between them would be smaller than the maximal size of a cross-section through the smallest of the two spheres. Although the coarse objects are generally not sphere-shaped, we still found this measure as useful. Two objects are thus merged if  $A_{AB} < \pi \cdot (\min(r_A, r_B))^2$ . In this case, the smaller fragment is assigned label ID of the larger fragment. Otherwise, the separation is retained.
3. Assignment of boundary voxels to avoid errors in the final volume measurements. If two objects are merged, the boundary voxels they share are assigned the same label. Otherwise, the boundary voxels are divided among both regions.

The result is a labeled image  $I_{Merge}$  containing the individual grains of the coarse fraction, identified by distinct label IDs.

### 4.3 Extraction of medium structures

The third part of our pipeline provides a method for extracting the grains of the medium structures. This part consists of two steps. In the first step, we create a binary image, containing only the medium fraction. In the second step, connected grains are separated.

#### *Removing coarse and fine structures*

In this step a binary image containing only the medium structures is created by removing the coarse and the fine structures from the segmented image  $I_{postS}$ . The coarse structures are removed by simply subtracting all foreground voxels in  $I_{Merge}$  from  $I_{postS}$ . The fine fraction is removed using an opening and a volume thresholding operation, as described for the removal of the medium structures in section 4.2. The threshold  $V_{medium}^{min}$  for removal is defined by the upper limit of the fine structures ( $150\mu\text{m}$ ). Thus, assuming a spherical shape and a resolution of  $35\mu\text{m}$ , objects up to a volume of 40 voxels will be removed. The result is a binary image  $I_{fRemove}$  which only contains the medium structures as foreground.

#### *Medium Splitting*

The visual analysis of the CT data shows that the medium grains are generally of roundish shape. For extracting such structures, we apply a method described in [35]. This method determines the regions of the objects and separates connected clusters when required. It is based on a marker-based watershed segmentation, which roughly works as follows (for details we refer to [35]):

1. The distance transformation [12]  $D$  is computed for all object regions. Thus, the value of each foreground voxel represents the distance to the nearest background voxel. Background voxels have value 0.
2. One marker, i.e. a voxel or a region of connected voxels, is computed for each grain (clusters of connected grains should obtain more than one marker, one for each grain). In principle, the markers are defined as the regional maxima of the distance transformation, i.e. the "object centers". However, spurious regional maxima can appear, due to contour irregularities and discretisation artifacts. This is avoided by first "shaving off" the regional maxima of the distance function and using the regional maxima of this smoothed distance function instead. This effectively reduces the number of markers by combining markers which are close to each other. This is efficiently implemented by computing the adapted distance field  $D' = D - 1$  and applying a gray-scale reconstruction by dilation operation of  $D'$  within  $D$  [34]. The latter operation can also be used to efficiently find the regional maxima [34].
3. Finally, the reduced set of markers is used for a marker-based watershed transformation [29]. Starting with the marker as initial labeled regions, these regions are expanded by iteratively adding neighboring voxels to all regions until the background or neighboring regions have been reached. Afterwards, each region represents an individual grain of the medium structures, together comprising the image  $I_{mSplit}$ .

#### 4.4 Result construction

From the extraction steps, we obtained the labeled images  $I_{Merge}$  and  $I_{mSplit}$  representing the coarse and medium grains. As the final step, we combine these results to obtain the image  $I_{Final}$  containing all extracted, uniquely labeled objects. The labels represent the positions and volumes of the grains. That forms the basis for the description of the grain structure by each grain.

## 5 Results

We prepared several samples as described in Section 3 and acquired CT images for all of them. The datasets have a size of approximately  $1800 \times 1800 \times 1800$  voxels (5 GB). We integrated the image processing pipeline of Section 4 into AMIRA [30]. Applying the full pipeline to one sample takes roughly five days on a high-end workstation with CPU Opteron 8220 (2.8 GHz) and 256 GByte of main memory. To date, we completely processed only a single data set.

For verification, the results of our image processing pipeline are compared with the volume distribution of the sieving data obtained from the dry sieving process (Section 3 and Figure 1). Therefore, we divide the extracted grains by their diameter into fractions according to the used sieve sizes. From image analysis the voxels of each grain are known. So, we can derive grain parameters like volume, position and diameter.

For a real sieving process it is assumed that elongated grains pass the sieves vertically. Thus, the diameter perpendicular to the first principal component is the used criterion to assign grains into the right fraction.

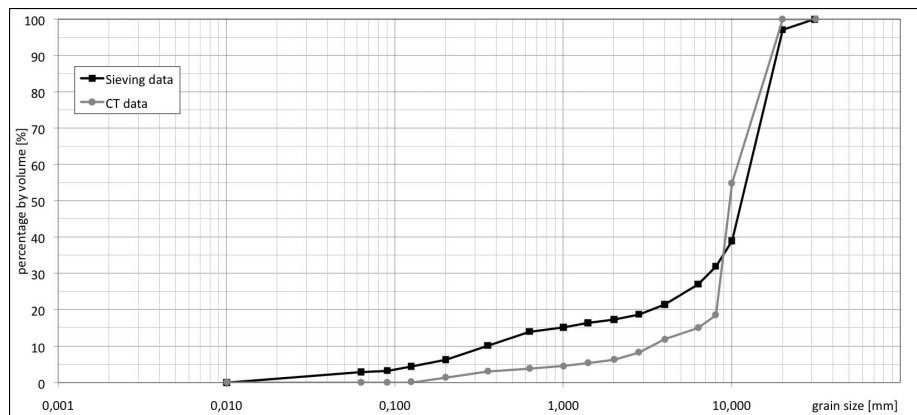
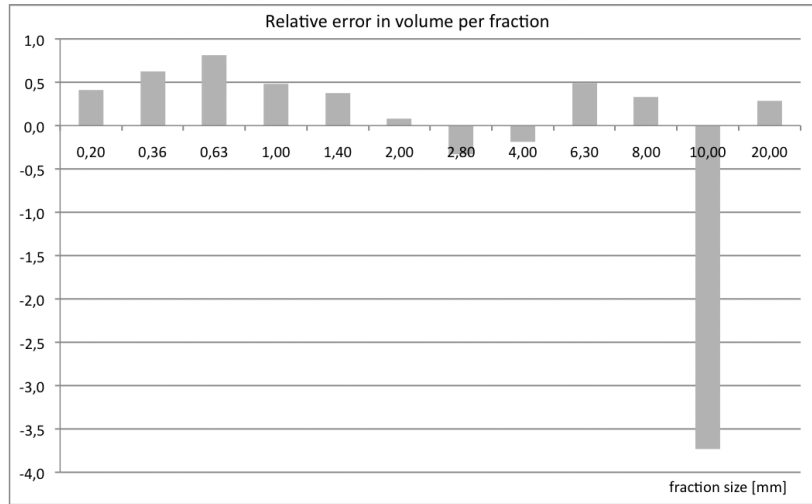


Fig. 4. Volume distribution of sieving data and CT data.

In order to get an approximation of the object diameters, we determine the extensions for each object by computing its tight-fitting bounding box [9], using an approach described in [21] which is based on the established *principal component analysis* [9]. Here, we first compute the principal axes of each object. These axes represent the object's directions of maximum extension. We assume the second principal direction to be the best description of the diameter of the objects. Rotating the principal axes in such a way that they are aligned with the axes of our standard coordinate system allows us to directly read off the extensions of the second direction. We use this extension as the diameter of the grains and for the grain fractionating. The validation of our fractionating was done by visually inspecting and manually measuring sample structures. The size of all structures classified in the fraction of 20 mm were determined using the 3D measuring tool of Amira that allows us to slice through the dataset and quantify the object extensions. In the same way we checked the size of five sample structures of the fraction 10 mm. The results showed that our diameter calculation for these grains and thus the fractioning for our data are correct. During the assignment of the grains into their fraction we accumulate the volume of grains per fraction. Thereof, we can derive the volume percentages for the volume distribution.

In Figure 4 the volume distributions of sieving data and CT data with all sieving fractions are shown. The gap between both curves represents the accumulated differences between the fractions. In Figure 5 the single relative errors of the extracted fractions are plotted. The positive bars refer to more sieved grains than extracted from CT data and reversed for negative bars. The variations may be caused by sources of error located in assumptions and elements of the presented pipeline as well as in the sample preparation. In our results, we differ three ranges of error.

1. We do not extract grains below 0.125 mm, while the sieve stack contains grains smaller than 0.10 mm. These fractions correspond to the group of fine structures defined initially. Because of the resolution limit the grains of these fractions are discarded from our pipeline. The distribution of the sieving data shows a small percentage for these small fractions. Thus, first differences in Figure 4 arise in fractions up to 0.125 mm.
2. The positive bars in Figure 5 for the fractions 0.2 to 0.63 mm refer to lower percentages of these fractions in the CT distribution than in the sieving distribution, i. e., the pipeline extracted less grains of these fractions than expected by the sieving distribution. This



**Fig. 5.** Relative error per extracted fraction of the sieving and the CT data. Positive bars refer to more sieved grains than extracted from CT data and reversed for negative bars.

may be caused by statistical deviations in the grain structure of the analysed sample as well as by mismatches in the segmentation and splitting process of our pipeline.

3. While the distributions for the lower fractions of the coarse structures possess similar trends, a large error for the fraction of 10 *mm* is mapped. The positive bar for the fraction of 20 *mm* marks a larger part in the sieving data than extracted from the CT data. Especially peculiar, the percentage of fraction size 20 *mm* is the most dominant part in the volume distribution of the sieving data and the percentage of the fraction of 10 *mm* takes a comparatively low part of the sieving distribution. In contrast the fractions of 10 and 20 *mm* in the CT distribution are almost similar. The negative bar for fraction 10 *mm* in Figure 5 shows that more grains with a size between 10 and 20 *mm* are extracted from the CT data than expected from the sieving distribution.

During the validation of our diameter determination by manual measuring, we found out that the percentage of grains of fraction size 20 *mm* is less than the percentage of the sieving distribution. Considering the relative error in Figure 5 for the coarse fractions, the grains of fraction size 20 *mm* may be underrepresented, respectively the grains of the 10 *mm* fraction may be overrepresented.

Certainly, the relative error of the fractions of 1–8 *mm* implies a large variation between sieving and CT data. However, these fractions form a small amount of the complete volume which is indicated by the low slope in the sieving distribution (Figure 4). These slopes are also present in the CT distribution. Herefrom, we conclude that the CT distribution reflects the trend of the sieving distribution for these fractions.

In case of the sieving data, the volume distribution is calculated from the mass distribution assigning a mean grain density of  $2.65 \text{ g/cm}^3$ . This may cause an additional source of error, we are not able to quantify.

To give a visual impression of the results, details of a 2D original slice and the corresponding result are shown in Figure 6. The detail represents a 2D area of  $10 \times 10 \text{ mm}$ . It contains

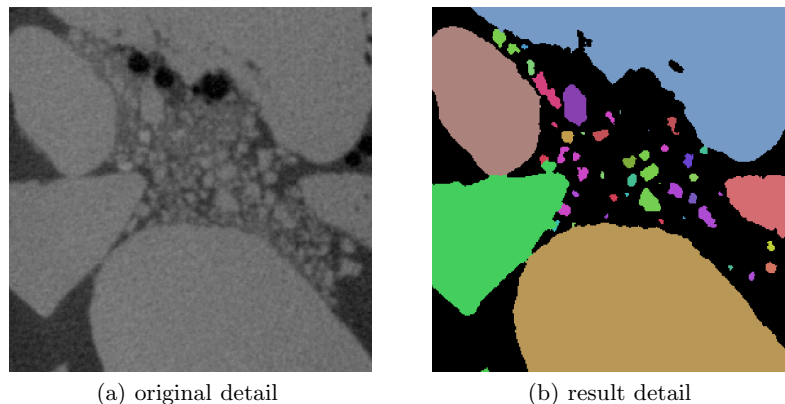


**Fig. 6.** Details of original and resulting data. The details show an area of  $10 \times 10 \text{ mm}$  containing grains of a size of 2 to 10  $\text{mm}$  at the boundaries and a cloud of grains with less than 1  $\text{mm}$  in the middle of the image.

grains of different sizes. A crowd of grains with a size less than 1  $\text{mm}$  is surrounded by grains between 2 and 10  $\text{mm}$ . The result (Figure 6(b)) represents the extracted grains marking their identity by different colors. As the result detail shows, the coarse grains are clearly splitted. Considering the original detail (Figure 6(a)), the crowd of fine and medium grains are closely together. The boundaries of these grains are blurred. Detecting these grains in our segmentation and medium splitting step may lead to an underestimation of the size or to a combination of single grains which results in an incorrect fraction assignment.

Finally, Figure 7 shows a 3D representation of the whole analysed dataset. All extracted grains are colored by their label ID assigned during the extraction process. As a result of the presented pipeline we get information about each extracted grain, e.g. its position and all voxels belonging to it. This allows us to describe the extracted grain structure as visualised.

## 6 Discussion

Considering the relative error plot, we have found that the extracted grains of the upper coarse fractions of size 10 and 20  $\text{mm}$  are not represented by the sample as expected from the sieving distribution. With a sample size of  $60 \times 60 \text{ mm}$  it is difficult to place a representative compound including grains of fraction size of 20  $\text{mm}$ . On the other hand, due to the cutting during the preparation process relative many coarse grains may be fragmented and therefore assigned into the lower fraction of 10  $\text{mm}$ . This results in shifted percentages of these fractions. While the percentage of the 20  $\text{mm}$  fraction shrinks, the percentage of the 10  $\text{mm}$  fraction grows, causing a difference with respect to the sieving distribution.

Furthermore, the grains of the medium fractions of 0.2 – 0.63  $\text{mm}$  are underestimated by the CT distribution. As shown in the result section, the segmentation might be one reason for the underrepresentation of the extracted medium grains. An insufficient segmentation result as input for the presented medium splitting method disables this method to extract the grains reliably. Potentially, the extraction of medium grains may be done with a shape model based approach that constrains the grains to ellipsoidal objects placed and sized by their gray values.

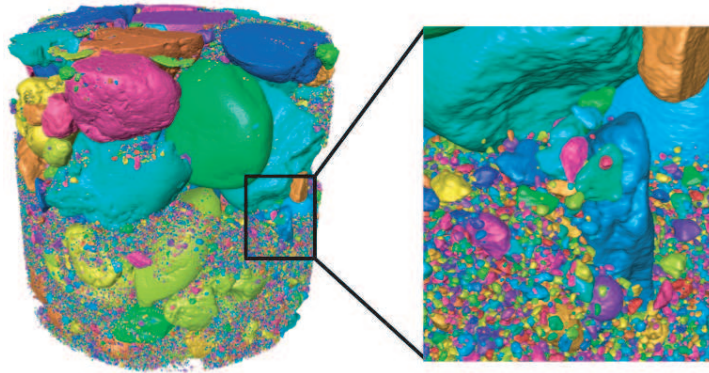


**Fig. 7.** Surface rendered result of the whole dataset. Each grain is colored by its label ID. The detail on the left points to extracted grains of different sizes.

For a better analysis of all fractions, we consider a multi level scanning approach in order to avoid boundary effects. First, a larger sample could be prepared and scanned as a whole at a lower resolution to ensure a representative compound including the upper coarse fractions. In further steps, that sample could be cut into smaller parts and scanned at a higher resolution in micro-CT. Thus, data are acquired at different resolutions for analysing grains of different sizes, which however would require the image processing task of registering the data.

Based on the results of our pipeline, we can describe the grain structure by the extracted grains depicted by their position, shape and volume. Figure 7 shows a 3D representation of the analysed dataset in which the grains are colored by their ID assigned during the extraction process. Even though the distributions of sieving and CT data differ, the visual observation has shown that the extraction of the grains of the coarse structures seems to be reliable and has to be verified by analysing a larger volume.

## 7 Conclusions

We have presented a promising approach for determining the geometric parameters of real gradated soil, suitable for analysing suffosion processes. Position, shape and volume of grains, can be used, for example, to validate modelling approaches, like [19, 20, 37]. Geometry of the coarse grains can be analysed to quantify pore structure. In this way, we can derive input parameters for percolation theory, which is an approach to analyse suffosion, as presented at this workshop [27].

First results indicate that our approach is feasible. Visual inspection reveals that sample preparation and data acquisition yield structures as expected in real soils. To some extent, our method can reproduce grain size distribution for coarse structures known from sieving. Based on the current results, the pore structure can already be preliminarily analysed for coarse grains. A larger amount of data is, however, needed to better understand deviations between sieving and micro-CT that is required to verify our approach.

Some more general questions also should be addressed before our approach becomes a reliable method that can provide parameters for validating suffosion criteria. First, we need to understand how CT in combination with image processing can be used to acquire the structure

of coarse grain in statistically large volumes, yet reach sufficiently high resolution for fine grains. Scanning the same specimen (or representative subsets) at different resolution and fusing the data might be a solution. Second, we need to improve handling of grains too small for the resolution of the tomogram. Maybe image processing can be improved, for example by incorporating prior knowledge, or fine grains can be omitted in a controlled way during sample preparation.

## Acknowledgements

This work is supported by the cooperation agreement of BAM and ZIB and partly funded by the German Research Foundation DFG in the project “SUFFOS” ([www.suffos.bam.de](http://www.suffos.bam.de)).

## References

1. R. Al-Raousha and K. A. Alshibli. Distribution of Local Void Ratio in Porous Media Systems from 3D X-Ray Microtomography Images. *Physica A*, 361(2):441–456, 2006.
2. V. V. Burenkova. Assessment of Suffosion in Non-Cohesive and Graded Soils. In U. Schuler, M. Heilbaum and J. Brauns, editors, *Filters in Geotechnical and Hydraulic Engineering on the First International Conference Geo-Filters, Karlsruhe, 20.-22. Oktober*, pages 357–367, Rotterdam, 1992. Balkema.
3. K. R. Castleman. *Digital Image Processing*. Prentice Hall, Inc., 1996.
4. R. P. Chapuis. Similarity of Internal Stability Criteria for Granular Soils. *Canadian Geotechnical Journal*, 29:711–713, 1992.
5. R. P. Chapuis, A. Constant and K. A. Baass. Migration of Fines in 0-20 mm Crushes Base During Placement, Compaction and Seepage under Laboratory Conditions. *Canadian Geotechnical Journal*, 33:168–176, 1996.
6. J. Čišťin. Zum Problem mechanischer Deformation nichtbindiger Lockergesteine durch die Sickerwasserströmung in Erddämmen. *Wasserwirtschaft Wassertechnik*, 2:45–49, 1967.
7. DIN 932-1. Prüfverfahren für allgemeine Eigenschaften von Gesteinskörnungen - Teil 1: Probenahmeverfahren. Technical report, Deutsches Institut für Normung e.V., Nov. 1996.
8. DIN 932-2. Prüfverfahren für allgemeine Eigenschaften von Gesteinskörnungen - Teil 2: Verfahren zum Einengen von Laboratoriumsproben. Technical report, Deutsches Institut für Normung e.V., Mar. 1999.
9. C. Ericson. *Real-Time Collision Detection*. Series in Interactive 3D Technology. Morgan Kaufmann Publishers, 2007.
10. A. M. Ghalib and R. D. Hryciw. Soil Particle Size Distribution by Mosaic Imaging and Watershed Analysis. *Journal of Computing in Civil Engineering*, 13(2):80–87, 1999.
11. L. Ibáñez, W. Schroeder, L. Ng, J. Cates, and the Insight Software Consortium. *ITK Software Guide*. Kitware, Inc., 2nd edition, 2005.
12. M. Jones, J. Baerentzen and M. Sramek. 3D Distance Fields: A Survey of Techniques and Applications. *IEEE Transactions on Visualizations and Computer Graphics*, 12(4):581–599, 2006.
13. A. Kaestner and P. Lehmann. Identifying the interface between two sand materials. In *Proceedings of the Fifth International Conference on 3-D Digital Imaging and Modeling (3DIM'05)*, 2005.
14. T. C. Kenney and D. Lau. Internal Stability of Granular Filters. *Canadian Geotechnical Journal*, 22:32–43, 1985.
15. H. Kim, C. T. Haas, A. F. Rauch, and C. Browne. 3D Image Segmentation of Aggregates from Laser Profiling. *Computer-Aided Civil and Infrastructure Engineering*, 18(4):254–263, 2003.

16. E. N. Landis and D. T. Keane. X-Ray Microtomography for Fracture Studies in Cement-Based Materials. In U. Bonse, editor, *Society of Photo-Optical Instrumentation Engineers (SPIE) Conference Series*, volume 3772, pages 105–113, Sept. 1999.
17. J. Löhrincz. On particle migration with the help of grading entropy. In M. Heibaum, U. Schuler and J. Brauns, editors, *Filters in geotechnical and hydraulic engineering on the first international conference Geo- Filters, Karlsruhe, 20.–22. Oktober*, pages 63–66, Rotterdam, 1992. Balkema.
18. E. A. Lubočkiv. The Calculation of Suffosion Properties of Non-Cohesive Soils when using the Non-Suffosion Analogue (russisch). In *International Conference on Hydraulic Research*, pages 135–148, Brno, Czechoslovakia, 1969.
19. E. Masad, C.-W. Huang, G. Airey and A. Muliana. Nonlinear viscoelastic analysis of unaged and aged asphalt binders. *Construction and Building Materials*, 22:2170–2179, Nov. 2008.
20. T. Mehlhorn, S. Prohaska and V. Slowik. Modelling and analysis of particle and pore structures in soils. In Witt K. J., editor, *Workshop Internal Erosion*, volume 21 of *Schriftenreihe Geotechnik*, November 2008.
21. B. Preim, H. Sonnet, W. Spindler, K. J. Oldhafer and H.-O. Peitgen. Interaktive und automatische Vermessung von 3D-Visualisierungen für die Planung chirurgischer Eingriffe. In *Bildverarbeitung für die Medizin*, number 19-23 in Informatik aktuell. Springer-Verlag, 2001.
22. M. Razavi, B. Muhunthan, and O. Hattamleh. Representative Elementary Volume Analysis of Sands Using X-Ray Computed Tomography. *Geotechnical Testing Journal*, 30(3):212–219, 2007.
23. S. A.-R. Saadeh. *Characterization of Asphalt Concrete Using Anisotropic Damage Viscoelastic-Viscoplastic Model*. PhD thesis, Texas A&M University, 2005.
24. U. Saucke. *Bewertung der Erosionsanfälligkeit strukturierter körniger Sedimente*. PhD thesis, Veröffentlichung des Institutes für Bodenmechanik und Felsmechanik, Universität Karlsruhe, 2004. Heft 162.
25. U. Schuler. How to Deal with the Problem of Suffosion. In *Research and Development in the Field of Dams*, Sept. 1995. 7.–9. September.
26. T. Schulz. *Einfluss von in situ-Randbedingungen auf die Feststoffeigenschaften von Dichtwandmassen*. Dissertation, Technischen Universität Carolo-Wilhelmina, 2002.
27. O. Semar and K. J. Witt. Modelling of suffosion processes with simulation in an uncorrelated bond-percolation model. page 10, Apr. 2008. Annual Meeting, European Working Group on Internal Erosion in Embankment Dams.
28. S. Shin and R. D. Hryciw. Wavelet Analysis of Soil Mass Images for Particle Size Determination. *Journal of Computing in Civil Engineering*, 18(1):19–27, 2004.
29. P. Soille. *Morphological Image Analysis: Principles and Applications*. Springer, Telos, 1999.
30. D. Stalling, M. Westerhoff and H.-C. Hege. Amira: A Highly Interactive System for Visual Data Analysis. In C. Hansen and C. Johnson, editors, *The Visualization Handbook*, pages 749–767. Elsevier, Salt Lake City, Utah, 2005.
31. J. Thieme, G. Schneider and C. Knöchel. X-ray tomography of a microhabitat of bacteria and other soil colloids with sub-100 nm resolution. *Micron*, 34:339–344, 2003.
32. P. R. Vaughan. Internal erosion of dams - assessment of risks. In *Filters and Drainage in Geotechnical and Environmental Engineering on the 3th International Conference Geofilters, Warszawa*, pages 349–356, Rotterdam, 2000. Balkema. inproceedings.
33. F. Verhelst, A. Vervoort, Ph. De Bosscher and G. Marchal. X-Ray Computerised Tomography, Determination of Heterogeneities in Rock Samples. In *Proceedings of the “8th International congress on rock mechanics (ISRM)*, pages 105–108, Tokyo, Japan, 1995.
34. L. Vincent. Morphological Grayscale Reconstruction in Image Analysis: Applications and Efficient Algorithms. In *IEEE Transactions on Image Processing*, volume 2 (2), pages 176–201, 1993.
35. L. Vincent and E. R. Dougherty. Digital image processing methods. *CRC*, 1994. in Digital Image Processing Methods.
36. H. Vogel. *Dränfähige Stabilisierungsinjektionen in erosions- und suffosionsanfälligen Lockergesteinen*. PhD thesis, Technische Universität Darmstadt, 1999.
37. L. Wang, J. Y. Park and Y. Fu. Representation of real particles for DEM simulation using X-ray tomography. *Construction and Building Materials*, 21(2):338–346, 02 2007.
38. L. B. Wang, J. D. Frost and J. S. Lai. Three-Dimensional Digital Representation of Granular Material Microstructure from X-Ray Tomography Imaging. *Journal of Computing in Civil Engineering*, 18(1):28–35, 2004.

39. J. Ziems. *Beitrag zur Kontakterosion nichtbindiger Erdstoffe*. PhD thesis, TU Dresden, 1969.
40. V. Y. Zou. Ein physikalisches Modell der pF-Kurve für teilgesättigte grobkörnige Böden. *Bautechnik* 80, pages 913–921, 2003. Heft 12.